Versatile Metamaterial: Exploring the Resonances of Symmetry-Protected Modes for Multitasking Functionality

Souhaïla Boublouh Miguel Suarez Feng Gao Abderrahmane Belkhir Abdelkrim Khelif Fadi Baida*

Souhaïla Boublouh
Institut FEMTO-ST, UMR 6174 CNRS, Département d'Optique P. M. Duffieux, Université de Franche-Comté, 25030 Besançon Cedex, France.
Email: souhaila.boublouh@femto-st.fr
Miguel Suarez
Institut FEMTO-ST, UMR 6174 CNRS, Département d'Optique P. M. Duffieux, Université de Franche-Comté, 25030 Besançon Cedex, France.
Email: miguel.suarez@femto-st.fr
Feng Gao
ZJU-Hangzhou Global Scientific and Technological Innovation Center, Zhejiang University, Hangzhou, China
Email: gao.feng@zju.edu.cn
Abderrahmane Belkhir
Laboratoire de Physique et Chimie Quantique, Université Mouloud Mammeri, Tizi-Ouzou, Algeria
Email: abderrahmane.belkhir@ummto.dz
Abdelkrim Khelif
Institut FEMTO-ST, UMR 6174 CNRS, Département MN2S, Université de Franche-Comté, 25030 Besançon Cedex, France
College of Science and Engineering, Hamad Bin Khalifa University, Doha, Qatar
Email: abdelkrim.khelif@femto-st.fr
Fadi Baida *
Institut FEMTO-ST, UMR 6174 CNRS, Département d'Optique P. M. Duffieux, Université de Franche-Comté, 25030 Besançon Cedex, France.
Email: fadi.baida@femto-st.fr

Keywords: *SP-BICs, Quasi-BICs, Infrared range*

In this article, we present an experimental study supported by numerical modeling that demonstrates the possibility of exciting Symmetry Protected-Bound states In the Continuum (SP-BICs) in a 1D silicon grating fabricated on a lithium niobate substrate. We investigate both transverse electric and magnetic polarization states, leading to the excitation of four quasi-Bound states In the Continuum (quasi-BIC) resonances, exhibiting distinct behaviors. Under standard illumination conditions (plane of incidence perpendicular to the 1D grating lines), two of these resonances are highly sensitive to illumination conditions, while the other two resonances involving unconventional illumination directions (plane of incidence parallel to the grating lines) are more robust to the angle of incidence, but just as sensitive to external stresses in terms of resonance wavelength and quality factor. Additionally, we experimentally demonstrate temperature detection with a sensitivity of $S_T = 0.81$ nm/°C, a state-of-the-art value achieved due to significant electromagnetic field enhancement inside the lithium niobate substrate at the quasi-BIC resonance. These findings pave the way for their use in various sensing applications (such as biology, electromagnetic, and temperature sensing), as well as nonlinear applications like second harmonic generation, and electro- and acousto-optic modulation.

1 Introduction

The enhancement of the light-matter interaction is a key point to exacerbate the optical response of a given structure, thereby improving its performance [1, 2]. To this end, two conditions must be fulfilled: first, increasing the lifetime of photons within the structure by exciting resonances with a high-quality factor (Q-factor), and second, ensuring strong confinement of the electromagnetic field at the sub-wavelength scale (small mode volume). The combination of these two conditions results in resonance with a large Purcell factor [3]. Otherwise, plasmonic resonances [4] may not be suitable in this context due to intrinsic absorption of used metals. Thus, most research teams today focus on dielectric structures [5] that fulfill the two conditions mentioned above. This can be achieved quite easily in some specific cases, such as the excitation of a frozen mode within a photonic crystal [6], a Fano-like resonance mode [7], a Guided

Mode Resonance (GMR) [8] or, more recently, a Bound state In the Continuum (BIC) [9]. In the latter case, these modes can be interpreted as non-radiative, resulting from destructive interference between two or more leaky modes, and thus they are not visible in optical spectra [10]. A typical example of such modes is the family of Symmetry Protected Modes (SPMs) [11]. The non-radiative character (dark modes) corresponds to resonance with an infinite Q-factor [9, 12]. Symmetry breaking allows the excitation of such modes, with a Q-factor becoming more important as the degree of symmetry breaking decreases [13]. Symmetry can be geometric (with respect to a specific axis or plane combined with an illumination having the same symmetry) or of electromagnetic origin (where geometric symmetry is maintained but the illumination differs in axis/plane of symmetry from the grating) [10]. BICs take part in many applications due to their extreme light confinement on a small scale and high sensitivity to slight external variations, such as changes in the refractive index of the medium. Typical applications include enhancing optical nonlinearities, where BICs can significantly improve the efficiency of various nonlinear optical phenomena, such as third harmonic generation THG in Si metasurfaces, or second harmonic generation SHG in non-centrosymmetric materials [14, 15] [16, 17].
In this paper, we propose a 1D sub-wavelength grating with simpler geometry than in most recent proposed configurations such as in [16, 17, 18], supporting multiple BICs and SPMs, not only in the near-infrared range or in the visible range [19] but also for different polarization states. The structure has been fabricated and characterized under various illumination conditions, revealing multiple resonances with a nearly high Q-factor. Numerical simulations using FDTD (Finite Difference Time Domain) are in excellent agreement with the experimental transmission spectra. The calculations also indicate that these high Q-factor resonances coincide with significant enhancement of the electric or/and magnetic fields, demonstrating strong electromagnetic field confinement either in the superstrate (air), substrate (lithium niobate), or within the structured medium itself. This suggests diverse applications such as biological detection (index variations), and in electro-, acousto- or pyro-electric modulation, with the same component operating at different wavelengths and under various illumination conditions.

2 Proposed geometry and results

As previously mentioned, to obtain SP-BICs, the structure must possess a high degree of symmetry. The simplest form is axial symmetry, which in the case of a 1D periodic lattice translates into plane (mirror) symmetry. Consequently, a rectangular cross-section ridge grating deposited on a planar substrate precisely meets this criterion, with axial symmetry perpendicular to the substrate interface.
The substrate chosen for this application is lithium niobate (LN), selected for its set of non-linear properties that make it electromagnetically very important. These properties include modulation of its optical refractive index (Pockel's effect or pyroelectric effect) and SHG enhancement, in response to various external stimuli. The nano-structure consists of an array of ridges made of amorphous silicon (Si), a dielectric material with a high refractive index in the near-infrared spectral range (NIR).
In order to operate in the vicinity of $\lambda = 1550$ nm, we proceeded to optimise the geometric parameters by performing simulations using a specially adapted FDTD code (see details in section 1 of Supplement 1). The aim of this parametric study was to find a structure that is easy to fabricate experimentally and that supports SP-BICs modes in the wavelength range of $\lambda \in [1200 - 1700]$ nm.
The geometrical characteristics of the structure after optimization, as depicted in Figure 1a, are as follows: the gap between ridges is $w = 60$ nm, their height is $h = 350$ nm, and the lattice period is $p = 640$ nm. These specific parameters enable the excitation of SP-BICs under different illumination conditions characterized by varying values of θ, ψ, ϕ (see Figure 1a), which denote angles specifying the illumination properties (direction and polarization). It is noted that the reference frame (x, y, z) aligns with the crystalline axes of the LN material for consistency of notations. As shown in Figure 1a, the LN substrate consists of an X-cut wafer, where the optical axis z is oriented parallel to the Si-ridges. This configuration exploits the lithium niobate's highest electro-optical coefficient r_{33} [20, 21, 22] when the incident plane wave is polarized along the z direction. Such alignment is crucial for achieving effective light-matter interaction. Fabrication was carried out using e-beam lithography technique as discussed in

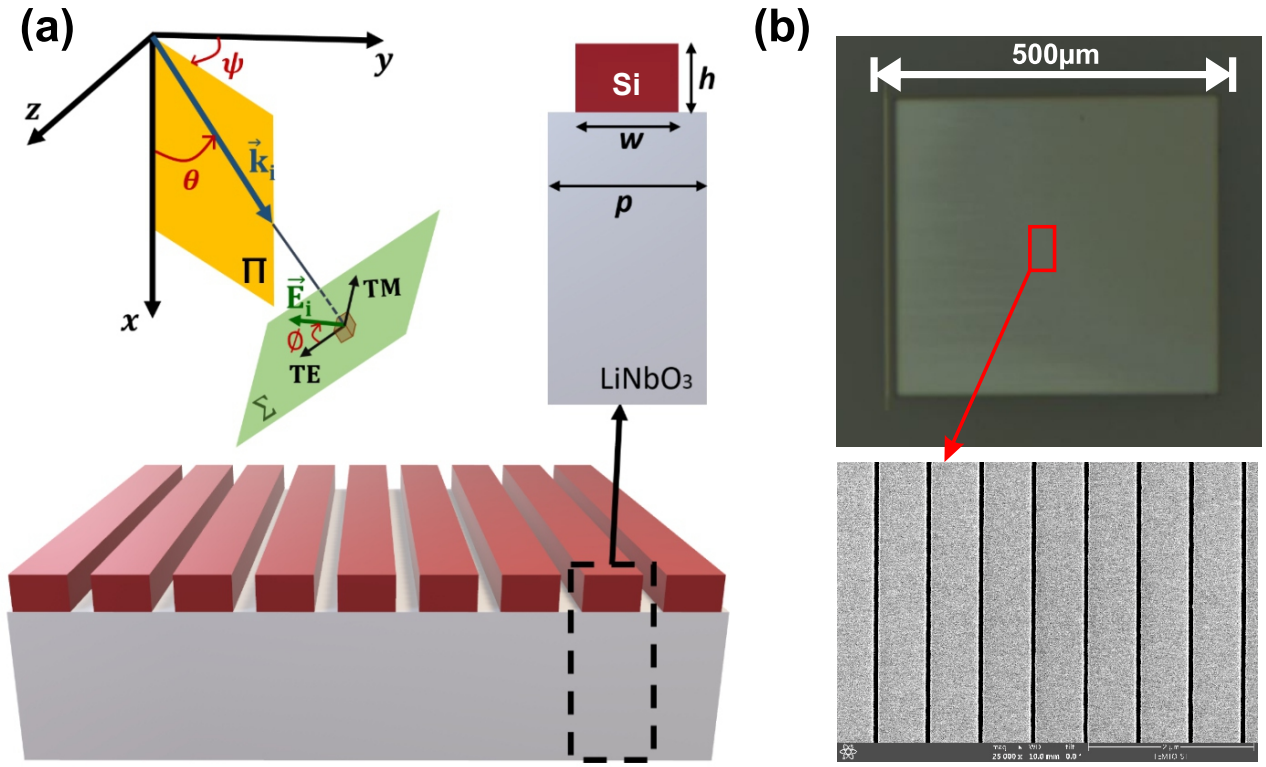

Figure 1: **a:** Illustration of the proposed grating design featuring Si-ridges atop an X-cut LN substrate. The grating parameters include the period $p = 640$ nm, ridge gap w = 580 nm, and ridge height $h = 350$ nm. Illumination characteristics are determined by three angles: the angles of incidence θ, azimuthal angle ψ, and the polarization angle ϕ. Π represents the plane of incidence, while the wavefront defined by the plane (TE,TM) is perpendicular to $\vec{k_i}$. **b:** Scanning electron microscope (SEM) image captured from the top view of the fabricated grating, with a magnified view showcasing the central portion revealing the individual ridges.

section 2 of Supplement 1. Figure 1b shows two scanning electron microscopy (SEM) images of the total manufactured structure (top), and a zoom-in (bottom) of the central part, revealing the high quality of the manufacturing process. Other SEM images are presented in Figure **S2** of Supplement 1, showing different steps to validate the good quality of the manufacturing.
Four distinct configurations were examined based on the direction and polarization of the incident plane wave. To distinguish them, we define three angles as depicted in Figure 1a : the azimuthal angle ψ, which specifies the angular orientation of the plane of incidence counted from the y axis, ϕ related to the polarization angle ($\phi = 0°$ for Transverse Electric (TE) and $\phi = 90\circ$ for Transverse Magnetic (TM) and the angle of incidence θ. Hence, the four configurations studied, both numerically and experimentally, correspond to the following parameters:
Configuration (a): $(\psi, \phi) = (0°, 0°)$
Configuration (b): $(\psi, \phi) = (0°, 90°)$
Configuration (c): $(\psi, \phi) = (90°, 0°)$
Configuration (d): $(\psi, \phi) = (90°, 90°)$
However, for all configurations, the illumination is conducted from above the grating (air) with the angle of incidence θ ranging from 0 to 30°. Notably, at normal incidence, configurations (a) and (b) are respectively equivalent to configurations (d) and (c). In the former case, the electric field aligns parallel to the Si-ridges (z - axis), while in the latter, it becomes perpendicular.
The optical refractive indices of LN are $n_x = n_y = n_o = 2.211$ and $n_z = n_e = 2.139$ [23]. Yet, only configuration (d) represents an anisotropic case, while both configurations (c) and (d) require 3D numerical simulations. The spectral positions of the Rayleigh anomalies (λ_A), the quality factor (Q) of resonances and their extinction ratio (ER) are also calculated (see section 2 of Supplement 1) to better understand some features of the transmission spectra. These anomalies may interfere with other resonant modes, thereby altering their properties. The experimental spectra are recorded using an adapted optical bench that has been specially developed for the occasion (see details in section 3 of Supplement 1).

2.1 Configuration (a): $(\psi, \phi) = (0°, 0°)$

In this configuration, the plane of incidence (xy plane) is perpendicular to the direction of the Si-ridges (z-axis). Moreover, the E-field is oriented along the z-axis ($\phi = 0°$), parallel to the Si-ridges. This corresponds to a conventional TE polarization case with no depolarization, as the plane of incidence is perpendicular to the direction of invariance (the z-axis). Consequently, the numerical simulations are entirely two-dimensional, reducing the electromagnetic field to only the (H_x, H_y, E_z) components.
Figure 2 illustrates both numerical (in **a**) and experimental (in **b**) results of the transmission angular diagrams. Note that the experimental ones are unprocessed raw data. Additionally, the Rayleigh anomalies of the diffracted first orders ($m = \pm 1$) are depicted by dashed blue lines in Figure 2a. There is excellent agreement between experiment and theory (Figure 2a and 2b) in terms of excited modes and resonance spectral positions.
Small differences can have several origins, such as the finite size of the structure and/or the illumination beam, as well as the unavoidable manufacturing defects. Under normal incidence ($\theta = 0°$), only the Guided Mode Resonance (GMR) is observable at the wavelength of $\lambda = 1368$ nm. However, a slight variation of the angle of incidence θ leads to a break, even slight, in the symmetry of the structure relative to the x-axis. Consequently, we observe the emergence of a Fano-shaped quasi-BIC above the $m = -1$ Rayleigh anomaly. This reveals the presence of a Symmetry Protected - Bound state in the Continuum (SP-BIC) at the point of high symmetry ($\theta = 0°$).
As the angle θ increases, the GMR experiences a blue shift, whereas the quasi-BIC undergoes a red shift. For example, Figure 2c illustrates the normalized transmission spectra obtained from both numerical simulation (black dashed line) and experimental measurement (red solid line) at the angle of incidence $\theta = 9°$. Within the same figure, one can observe the presence of the two resonances: the GMR located around $\lambda = 1330$ nm and the quasi-BIC at $\lambda = 1477$ nm. Beyond $\theta \approx 13°$, the SP-BIC couples destructively with the Rayleigh anomaly of order $m = -1$. This leads to an increase in its quality factor before it disappears completely, giving rise to an accidental BIC [24].

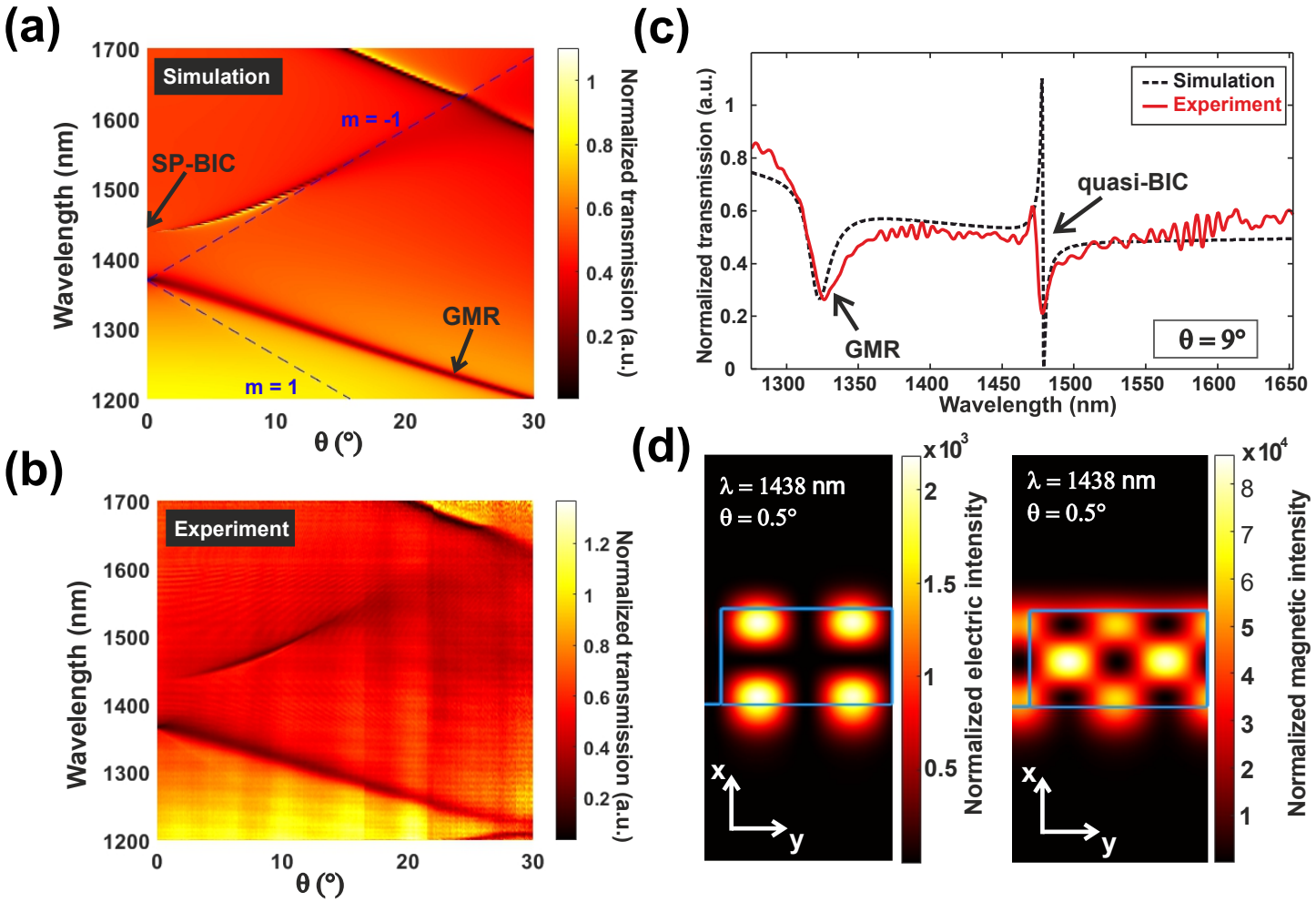

Figure 2: **a:** Transmission angular diagram obtained by FDTD numerical simulations. **b:** The dashed blue lines represent the positions of the Rayleigh anomalies for both the $m = 1$ and $m = -1$ diffraction orders. Transmission in diagram obtained from experimental measurements. **c:** The transmission spectra acquired from simulation (black dashed line) and experiment (red solid line) at the angle of incidence $\theta = 9°$. **d:** Distributions of the normalized electric and magnetic intensities obtained from FDTD simulations at the spectral position of the quasi-BIC $\lambda = 1438$ nm for an incidence angle of $\theta = 0.5°$.

To further explore the quasi-BIC properties, we examine a small angle of incidence, for instance, $\theta = 0.5°$, for which the quasi-BIC resonates at a wavelength of $\lambda_{num} = 1438$ nm, exhibiting a substantial Q-factor of $Q_{num} = 10^6$. We numerically demonstrate that this resonance is accompanied by a significant enhancement of both electric and magnetic field intensities (see definitions in section 2 of Supplement 1), with values of $I_e = 2.10^3$ and $I_m = 8.10^4$, respectively, as illustrated in Figure 2d. Based on these results, the quasi-BIC could be ideally suited for a wide range of integrated photonics applications, particularly in areas such as opto-electronics [25, 11] and nonlinear optics [26, 27].From these two field distributions in Fig. 2d, the quasi-BIC appears to have a magnetic quadrupole origin, with an exaltation of the magnetic field 40 times greater than that of the electric field. We have numerically verified that another mode, i.e. magnetic dipolar, does exist and emerges at a higher wavelength of the order of $\lambda = 1940$ nm. Further investigations show that the origin of these modes may be linked to Mie-type resonances for which the resonance wavelengths would be strongly red-shifted due to periodicity compared to that of a single Si-ridge. The fact that the electric field of the electromagnetic wave is polarised along the LN's crystalline axis (z-axis) makes the configuration highly compatible with electro-optical or pyroelectric applications. Indeed, the largest electro-optic (EO) coefficient of the LN is $r_{33} = 31$ pm/V [28], which is mainly involved in the Pockel's effect in this case. The obtained variation in the refractive index

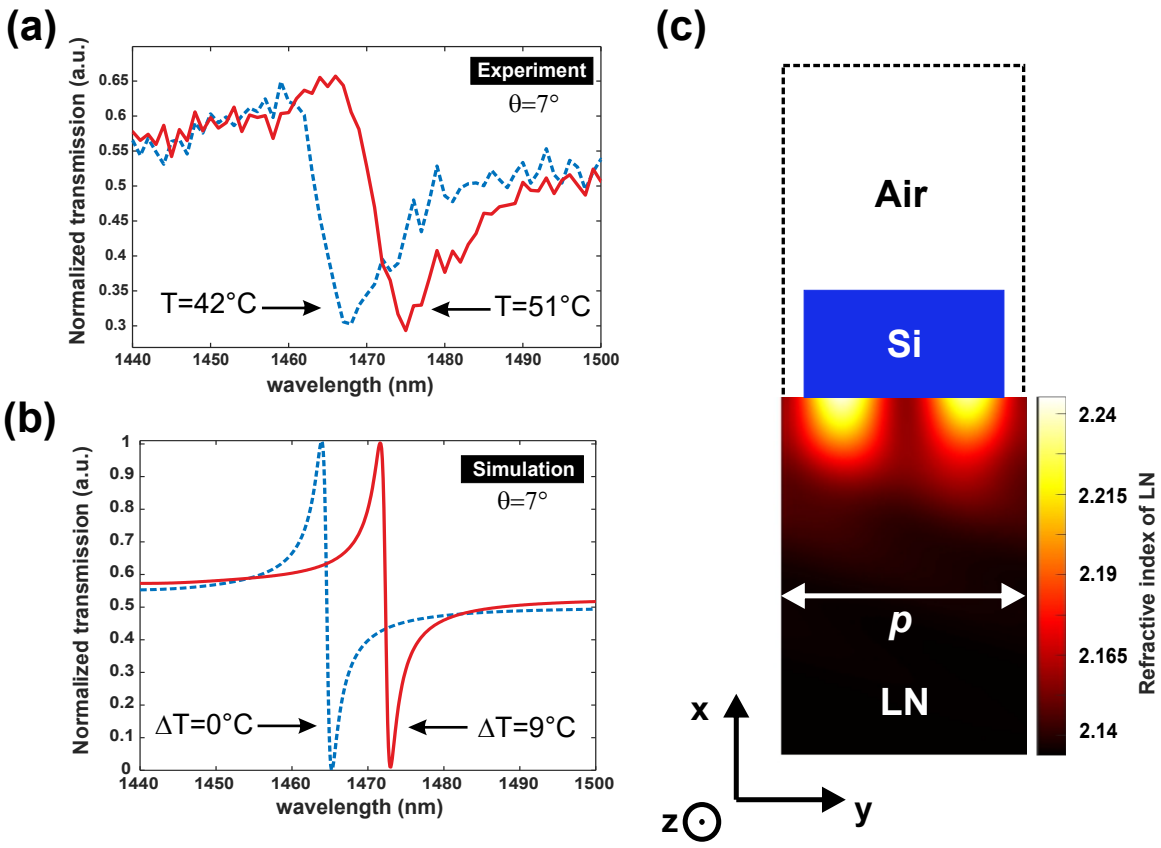

Figure 3: **a:** Experimental normalized transmission spectra around the quasi-BIC resonance at two room temperatures, $T = 42°\text{C}$ (blue dashed line) and $T = 51°\text{C}$ (red solid line), for a TE polarized illuminating plane wave with an angle of incidence $\theta = 7°$. **b:** Numerical transmission spectra around the quasi-BIC calculated by FDTD for the case of no temperature change $\Delta T = 0°\text{C}$ (blue dashed line) and at temperature change $\Delta T = 9°\text{C}$ (red solid line) calculated at the angle of incidence $\theta = 7°$. **c:** Refractive index distribution over one period of the structure corresponding to a temperature variation of $\Delta T = 9°\text{C}$. This is calculated using Eq.3 after FDTD simulations , which allow calculation of $f(x, y)$ at the quasi-BIC resonance wavelength.

is given by Equation 1 [11] below.

$$\Delta n(x, y) = -\frac{1}{2} n_e^3 r_{33} f(x, y)^2 E_s \tag{1}$$

$$E_s = -\frac{1}{\varepsilon_0 \varepsilon_r} p_t \Delta \text{T} \tag{2}$$

Here, E_s denotes the external applied electric field magnitude, ε_0 and ε_r are, respectively, the vacuum and the LN relative dielectric constants equal to $\varepsilon_0 = 8.854 \times 10^{-12}$ F/m, and $\varepsilon_r = 28.7$. The function $f(x, y)$ represents the local optical field factor computed at each FDTD cell. It quantifies the electric field amplitude in the presence of the grating relative to the field amplitude in the absence of the grating. However, this refractive index modification can also be induced by a change in temperature (pyroelectric effect), which, through induced polarization, results in the generation of a charge displacement leading to an electric field (polarization) within the LN crystal. A relationship linking the two effects is given by Equation 2, where p_t is the pyroelectric coefficient of the LN, $p_t = -8 \times 10^{-5}$ $\text{Cm}^{-2}\text{K}^{-1}$ [29], and ΔT corresponds to the temperature variation in Celsius (or Kelvin).
By injecting Equation 2 into Equation 1, we obtain the expression of the local refractive index modification due to a temperature change of ΔT as:

$$\Delta n(x, y, \Delta T) = \frac{n_e^3 r_{33} p_t}{2\varepsilon_0 \varepsilon_r} f(x, y)^2 \Delta \text{T} \tag{3}$$

The modification of the refractive index is then calculated through Equation 2 for each FDTD-cell of the mesh and incorporated into the FDTD simulations to estimate the effect on the transmission response.

Using a Peltier heater installed close to the structure, we first increased its temperature to 42°C and left it to stand for six hours to eliminate the polarization induced by this heating. We then increased the temperature to 51°. For each temperature, a spectral measurement was made around the quasi-BIC resonance. The results are shown in figure 3a, where the dashed blue spectrum corresponds to room temperature $T = 42°\text{C}$ while the solid red corresponds to $T = 51°\text{C}$. To compare with theory, we first recalculated the homogeneous LN with an index of 2.139 and then determined from equation 3 the cell-by-cell variations in LN refractive index due to a $\Delta T = 9°\text{C}$ (see Figure 3b). The theoretical spectra presented in Figure 3b are in almost perfect agreement with the experiment, where a shift of $\Delta\lambda = 7.3$ nm is obtained instead of $\Delta\lambda = 7.65$ nm in theory. These two values are in a great agreement, leading to an experimental measured thermal sensitivity of $S_t = \frac{\Delta\lambda}{\Delta T} = 0.81$ nm°C^{-1}. This value is amazingly similar to values obtained in previous studies [30].

2.2 Configuration (b): $(\psi, \phi) = (0°, 90°)$

In this configuration, the plane of incidence remains the same as in configuration (a), namely perpendicular to the Si-ridges. However, the polarization state changes to a transverse magnetic (TM) with $\phi = 90°$. Consequently, the electromagnetic field components are now characterized by (E_x, E_y, H_z), where the electric field aligns with both ordinary axes (x and y), resulting in an isotropic study case. Numerical simulations and experimental measurements of the transmission angular diagram are presented in Figure 4a and Figure 4b, respectively. As before, the Rayleigh anomalies are also indicated by the blue dashed lines. In both diagrams, we observe the emergence of a quasi-BIC above the Rayleigh anomalies when the angle of incidence increases, leading to its apparition at approximately $\lambda = 1678$ nm. The numerical and experimental normalized transmission spectra at an angle of $\theta = 4°$ are illustrated in Figure 4c, where the quasi-BIC is located at a wavelength of $\lambda = 1686$ nm. In contrast to configuration (a), the quality factor of the SP-BIC decreases considerably with small symmetry breaks, giving rise to a broadened resonance. To exploit it in detection, modulation, or non-linear signal generation applications, it would be necessary to operate at small incidence angles. Therefore, to quantify the confinement of the electromagnetic field, we consider an angle of incidence $\theta = 0.5°$ for which the mode appears at $\lambda = 1679$ nm with a Q-factor of $Q = 892$. As depicted in Figure 4d, the electric intensity associated with the mode is predominantly enhanced at the surface of the LN substrate within the air cavities, reaching a maximum of $I_e = 6 \times 10^3$, along with an enhancement in magnetic intensity, mainly confined inside the Si-ridges, peaking at $I_m = 3 \times 10^4$. As for configuration (a), we observe a strong increase in magnetic intensity, probably due to the excitation of a Mie-type magnetic dipolar resonance (no other resonances at longer wavelengths) of the Si-ridges, which considerably increases the MLDOS (local density of magnetic states), opening the way to magneto-optical applications with non-absorbing structures [31, 32] other than metallic nano-antennas [33]. As mentioned above, the electric field at resonance is significantly enhanced at the substrate interface between two Si-ridges in the gap region. This enhancement could be exploited to build a bio-sensor or refractive index detector. In this case, the superstrate is no more air but a liquid (water or blood) with refractive index n_l. FDTD simulations were conducted using two fairly close values of n_l to evaluate the refractive index sensitivity of the structure in the vicinity of the quasi-BIC. Figure 5a shows the obtained transmission spectra in the spectral region of the quasi-BIC resonance for $n_l = 1.34$ and $n_l = 1.35$, with the angle of incidence from air on the liquid interface fixed to $\theta = 0.75°$. We can clearly see that the transmission peak is slightly shifted by $\Delta\lambda = 0.7$ nm corresponding to a weak sensitivity of 70nm/RIU, which is not sufficiently relevant for a refractive index detection, even though the Q-factor of the resonance is quite high ($Q = 490$). Nevertheless, phase detection, as opposed to intensity detection, can greatly improve sensitivity in certain configurations [34]. Figure 5b presents the corresponding phase change induced during the transmission of light through the structure for the same two values of the refractive index (dotted blue line for $n_l = 1.34$ and solid black line for $n_l = 1.35$). At $\lambda = 1693.95$ nm, the phase difference, plotted as a green dashed line, is maximized at 23.48°, providing a good phase sensitivity of 2348°/RIU. This value is considerably high [35, 36], making the structure an excellent candidate for various applications, including label-free bio-sensing, bio-imaging, and optical filters.

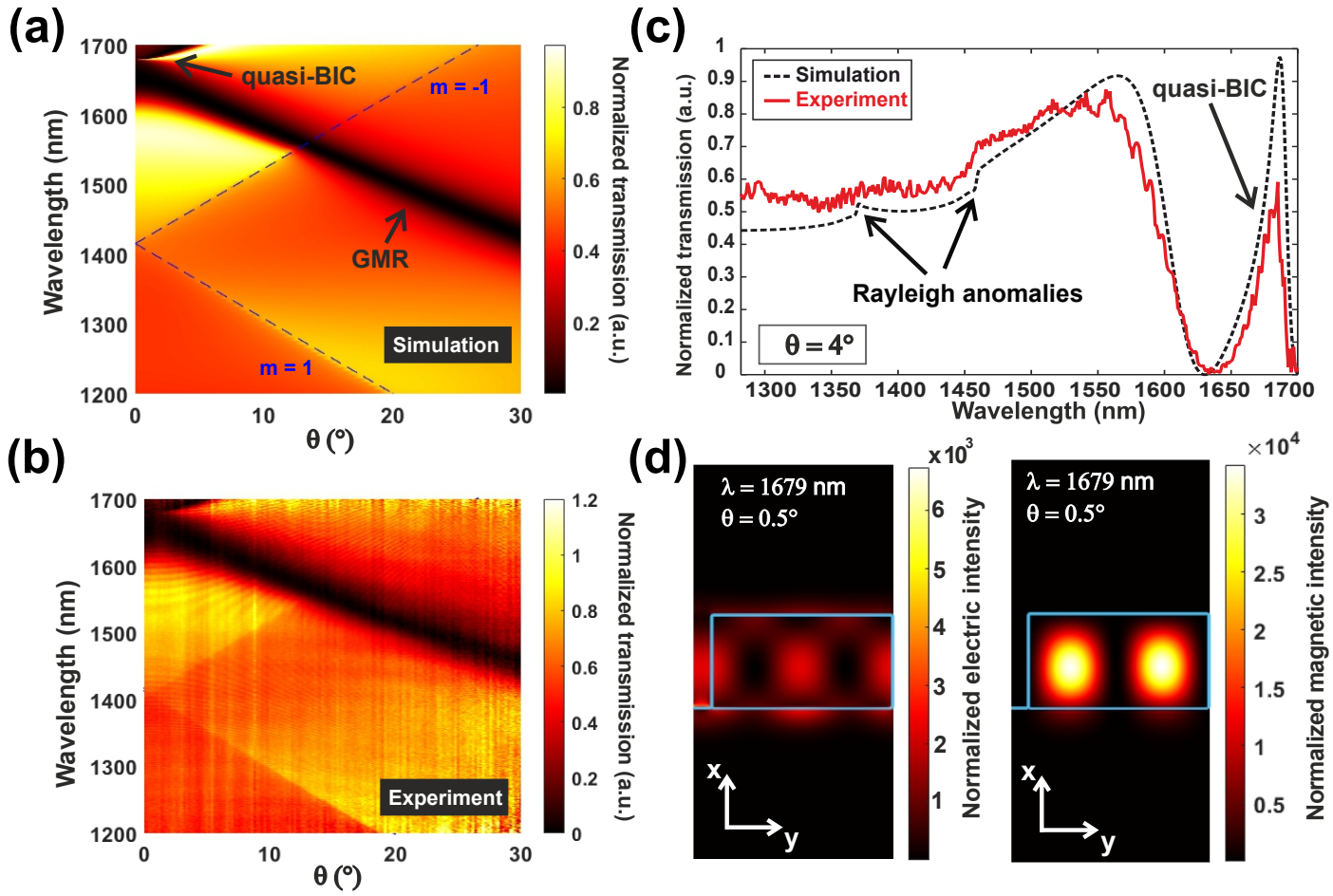

Figure 4: Transmission angular diagram derived from FDTD numerical simulations in **a**. The dashed blue lines represent the spectral positions of the Rayleigh anomalies for both the $m = 1$ and $m = -1$ diffraction orders. Transmission angular diagram obtained from experimental measurements in **b**. The transmission spectra acquired from simulation (black dashed line) and experiment (red solid line) at the angle of incidence $\theta = 4°$ are both presented in **c**. Distributions of the normalized electric and magnetic intensities, in **d**, obtained from FDTD simulations at the spectral position of the quasi-BIC $\lambda = 1679$ nm for an incidence angle of $\theta = 0.5°$.

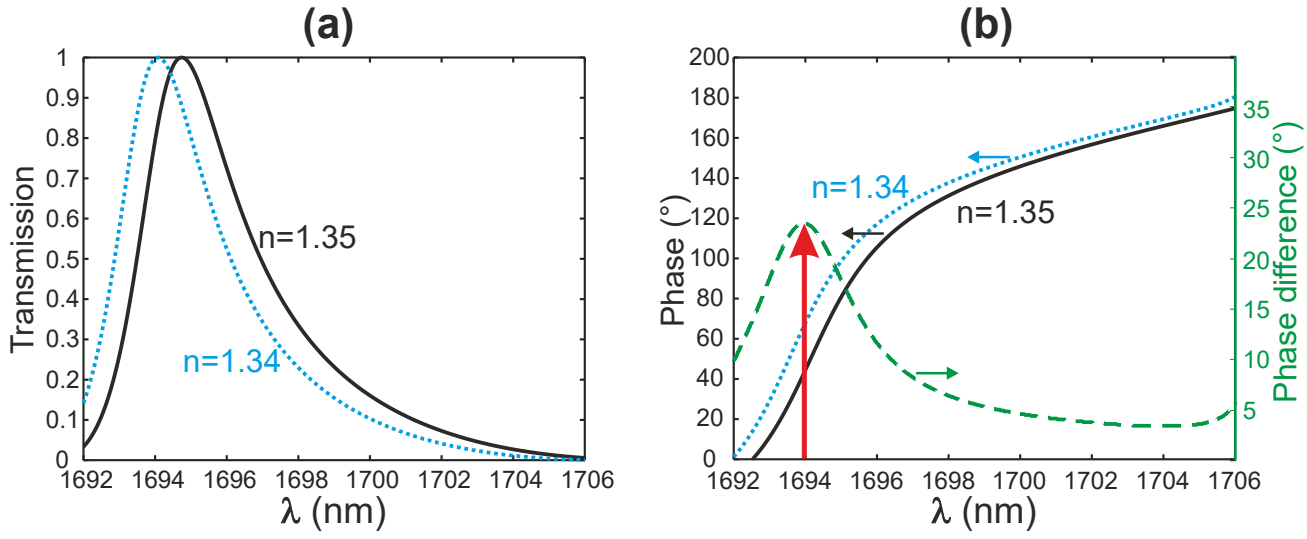

Figure 5: **a:** Transmission spectra in the region of the quasi-BIC of the structure with two different values of the refractive index n_l of the liquid superstate ($n_l = 1.34$ in dotted blue line and $n_l = 1.35$ in solid black line). **b:** Corresponding phase changes of the transmitted electric fields for the two values ($n_l = 1.34$ in dotted blue line and $n_l = 1.35$ in solid black line). The phase difference is plotted in dashed green line with a maximum value indicted by the vertical red arrow corresponding to 23.49° at $\lambda = 1693.95$ nm.

2.3 Configuration (c): $(\psi, \phi) = (90°, 0°)$

In this configuration, the azimuthal angle ψ is set to 90°, corresponding to a plane of incidence that is parallel to the xz plane and aligned with the Si-ridges. The polarization is set to TE ($\phi = 0°$), ensuring that the electric field remains perpendicular to the Si-ridges, regardless the angle of incidence. Due to the diffraction and the invariance along the z direction, this electric field will produce a field only located in the xy plane, making the theoretical problem completely isotropic. Additionally, as in configuration (d), changing the angle of incidence induces a very slight change in illumination conditions, so this case is rarely considered in the literature.

The numerical and experimental transmission angular diagrams are illustrated in Figure 6a and 6b, respectively. Once again, the simulations yield results that are very faithful to those obtained experimentally (see Figure 6c), showing the excitation of one SP-BIC mode and one GMR. These two modes are the same as those obtained in configuration (a) for the quasi-BIC and in configuration (b) for the GMR. In fact, at normal incidence, configuration (c) is completely identical to configuration (b), while the occurrence of quasi-BIC is due to the diffraction-induced depolarization at $\theta \neq 0°$, specifically the emergence of a non zero x-component of the electric field. As expected, the weak extrinsic symmetry break ($\theta \neq 0$) reveals this quasi-BIC at the same wavelength as in configuration (a), above the Rayleigh anomaly, as depicted in Figure 6c for $\theta = 9°$. The quasi-BIC resonance exhibits a good quality factor over a wide range of angle of incidence (up to $Q_{num} = 0.94 \times 10^6$ for $\theta = 0.5°$), making this configuration more robust with respect to the experimental illumination conditions.

At the aforementioned quasi-BIC resonance, the electromagnetic field distributions (Figure 6d) are obviously similar to those in configuration (a) (Figure 2d), but with a slightly higher enhancement, as shown on Figure 6d. The normalized electric and magnetic field intensities reach $I_e = 9 \times 10^3$ and $I_m = 8 \times 10^4$, respectively, for $\theta = 2°$, whereas similar enhancement factors require a smaller angle of incidence ($\theta = 0.5°$) in the configuration (a). Nevertheless, even though the origin of the quasi-BIC is the same (Mie-type magnetic resonance) for both configurations (a) and (c), the spectral behavior with respect to variation in the angle of incidence is different. Specifically, for the (c) configuration, increasing the grating's asymmetry induces a blue-shift to the quasi-BIC, while it red-shifts in configuration (a). Furthermore, the potential applications of the quasi-BIC generated in this configuration are very similar to those proposed in configuration (a) due to their comparable confinement properties. However, at high incidence angles ($\theta > 4°$), the quasi-BICs in the two configurations occupy different spectral positions and can therefore be used simultaneously for the same or different applications, depending on the desired performance of each.

2.4 Configuration (d): $(\psi, \phi) = (90°, 90°)$

In this last configuration, both angles ψ and ϕ (defined in Figure 1a) are set to 90°. Therefore, the plane of incidence is the xz plane, as in configuration (c) but the polarization state is TM. Consequently, the electric field is parallel to the plane xz and now has two components along both the ordinary and extraordinary axes (x and z). The 3D-FDTD simulations must account for this anisotropy in this configuration. The numerical and experimental transmission angular diagrams are presented in Figure 7a and 7b respectively. As before, there is a good agreement between the two results. In Figure 7a, the dashed blue line identifies the Rayleigh anomaly corresponding to the first diffracted order ($m = \pm 1$), calculated using Equation S1 of Supplement 1. Both diagrams emphasize the presence of two modes. However, under normal incidence, this configuration is identical to configuration (a), where a single mode exists above the Rayleigh anomalies, which is actually the GMR at $\lambda = 1370$ nm. The second mode, which is more difficult to observe experimentally, only appears at $\theta \neq 0°$, presenting an exceptional quality factor of $Q_{num} = 1.3 \times 10^6$ at $\theta = 0.5°$, indicating a quasi-BIC state. This reveals the presence of an SP-BIC at the highest symmetry point (here Γ).

Nevertheless, the excitation of the BIC is clearly visible on the two diagrams in Figures 7a and 7b, but their extinction ratio is different. The blatant discrepancy between the theoretical and experimental quality factors clearly demonstrates the sensitivity of the structure to manufacturing defects when the plane

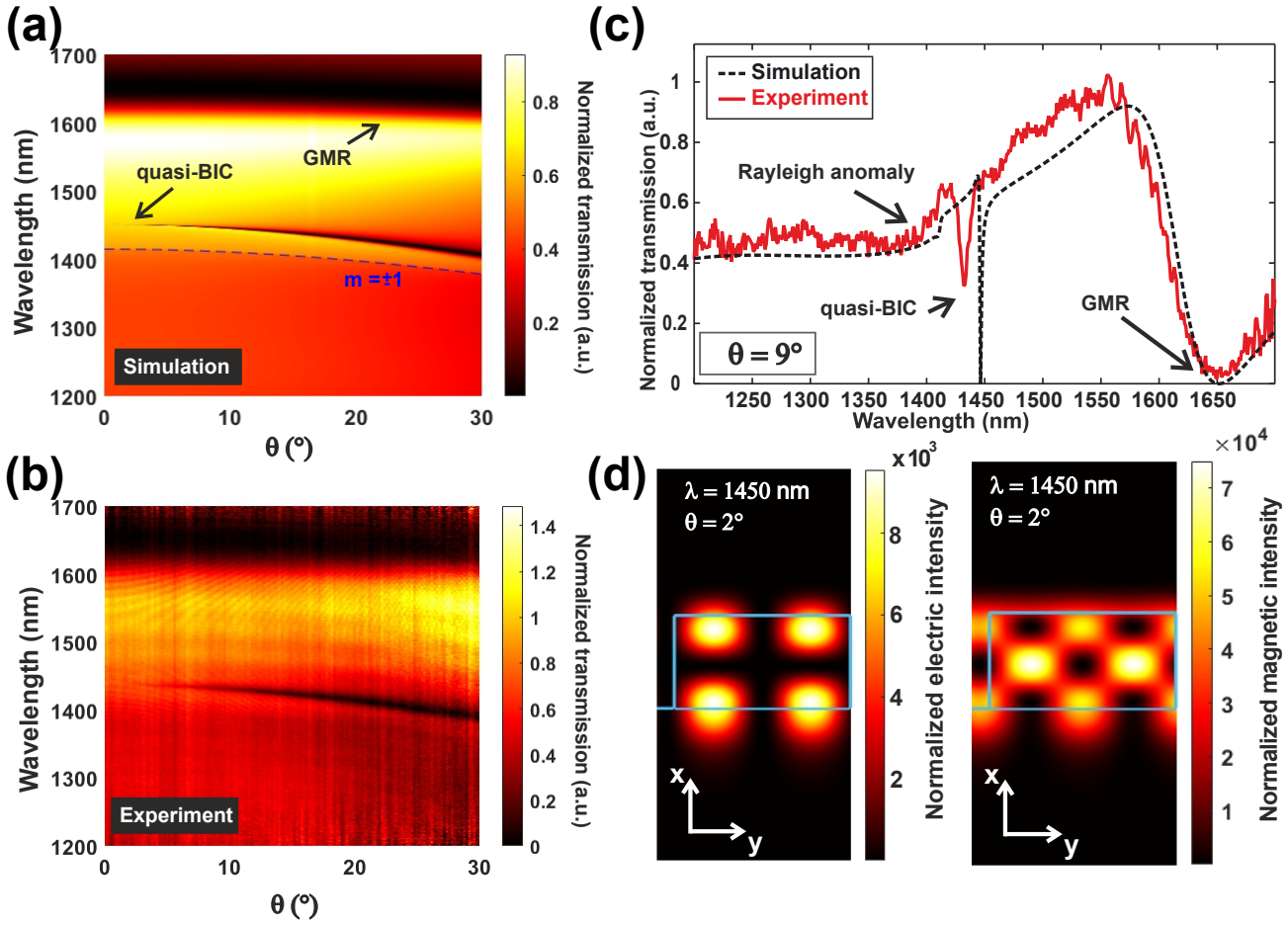

Figure 6: **a:** Transmission angular diagram derived from FDTD numerical simulations. The dashed blue line represents the spectral positions of the Rayleigh anomaly for the first diffracted order ($m = \pm 1$). **b:** Transmission angular diagram obtained from experimental measurements. **c:** The transmission spectra obtained from simulation (black dashed line) and experiment (red solid line) at the angle of incidence $\theta = 9°$. **d:** Distributions of the normalized electric and magnetic intensities obtained from FDTD simulations at the spectral position of the quasi-BIC $\lambda = 1450$ nm for an incidence angle of $\theta = 2°$.

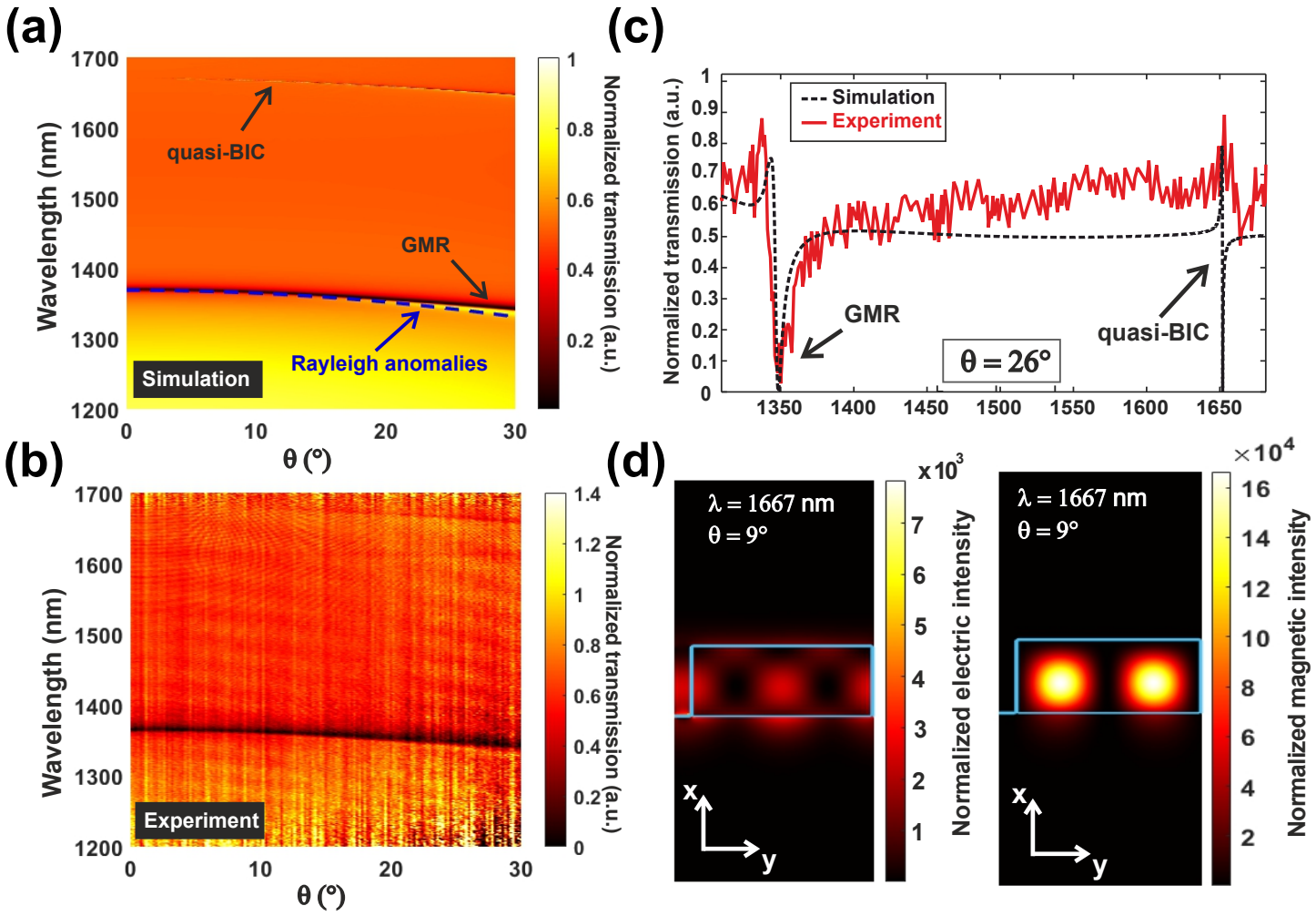

Figure 7: **a:** Transmission angular diagram derived from FDTD numerical simulations. The dashed blue line represents the spectral positions of the Rayleigh anomaly for the first diffracted order ($m = \pm 1$). **b:** Transmission angular diagram obtained from experimental measurements. **c:** The transmission spectra acquired from simulation (black dashed line) and experiment (red solid line) at the angle of incidence $\theta = 26°$. **d:** Distributions of the normalized electric and magnetic intensities obtained from FDTD simulations at the spectral position of the quasi-BIC $\lambda = 1667$ nm for an incidence angle of $\theta = 9°$.

of incidence and the electric field of the incident wave are both parallel to the ridges of the grating. This difference may also be linked to the fact that the wavelength of the quasi-BIC is very close to that of the Rayleigh anomaly, as shown in Figure 7a. Combined with manufacturing defects (mostly related to ridge width), this could lead to a widening of the resonance as shown in Figure 7c.
However, this makes this configuration one of the most suitable for detecting small changes in the geometry of the structure, as will be demonstrated in the following through the considered opto-mechanical application.
As with configuration (c), quasi-BIC maintains a significant quality factor even at higher angles of incidence. For example, at $\theta = 26°$ its value remains substantial (see Figure 7c), reaching a theoretical value of $Q_{num} = 0.57 \times 10^4$, with a perfectly asymmetric Fano-shape, making this configuration highly promising for lasers and Q-switch applications.
Moreover, this quasi-BIC is the same as the one excited in configuration (b) at around $\lambda = 1679$ nm and is due to depolarization, which reveals a y-component that remains fairly weak regardless the angle of incidence. Figure 7d illustrates the electric and magnetic intensity distributions for $\theta = 9°$. As expected, these distributions are identical to those of the quasi-BIC achieved in configuration (b). However, the quasi-BIC generated in this configuration offers better confinement due to its high Q-factor and has the advantage of being more robust with respect to the angle of incidence.
By observing the symmetry of the electric field distribution in Figure 7d, we can see that it is closely dependent on the shape of the Si-ridge. A mechanical vibration of this ridge is likely to disrupt the excitation of this quasi-BIC by shifting its excitation wavelength, which will modulate the intensity of the transmitted signal. Consequently, we investigate the structure‘s sensitivity to such mechanical vibration, which is particularly relevant for acousto-optical applications [37].
A straightforward approach is to consider a uniform tilt of the Si-ridge as shown in Figure 8a, where α denotes the tilt angle of the ridge relative to the vertical direction. To estimate the influence of ridge bending, we calculated the transmission spectrum for $\alpha = 1°$ (corresponding to a maximum displacement of 6.1 nm for the top of the ridge) and compared it to that of the initial structure ($\alpha = 0°$). Both spectra are shown in Figure 8b, where the quasi-BIC undergoes a shift of $\Delta\lambda = 3.3$ nm, leading to a sensitivity of $\dfrac{\Delta\lambda}{\Delta\alpha} = 3.3$ nm/degree. We believe that this bending can be induced by a surface acoustic wave (SAW), directed along the y-axis and generated by an interdigital comb arranged alongside the structure, on the surface of the LN piezoelectric substrate.

3 Conclusion

We have demonstrated the ability to excite quasi-BIC modes by symmetry breaking, using four distinct configurations within the same simple-to-fabricate structure that does not involve lithium niobate structuring. By breaking the lattice symmetry, leakage to the SP-BIC occurs, resulting in a resonant mode (quasi-BIC) within the lattice with a particularly high Q factor. Numerical simulations and experimental measurements show excellent agreement, confirming the reliability of the proposed structure. In each configuration, the investigation of quasi-BIC demonstrated the quality of the electromagnetic field confinement. Of the four configurations, only two SP-BICs exist, but their coupling to the continuum can occur in two distinct ways. For example, while configurations (a) and (c) differ in various aspects such as plane of incidence, LN's refractive index, and levels of symmetry breaking, they both produce quasi-BICs with similar characteristics, including comparable wavelengths at low angles of incidence ($\theta \leq 0.5°$) and similar field distributions. This similarity allows for their exploitation under different experimental conditions, as schematically shown in Figure 9. Similarly, configurations (b) and (d) exhibit similarities in their quasi-BICs excited at low angles of incidence ($\theta \leq 0.5°$), indicating the common origin of the SP-BIC. However, the four generated quasi-BICs show distinct responses to increasing asymmetry via the angle of incidence.
In addition to the compact size of the structure and the absence of etching in the LN, all quasi-BICs offer significant light confinement, making the proposed structure an efficient miniaturized device for in

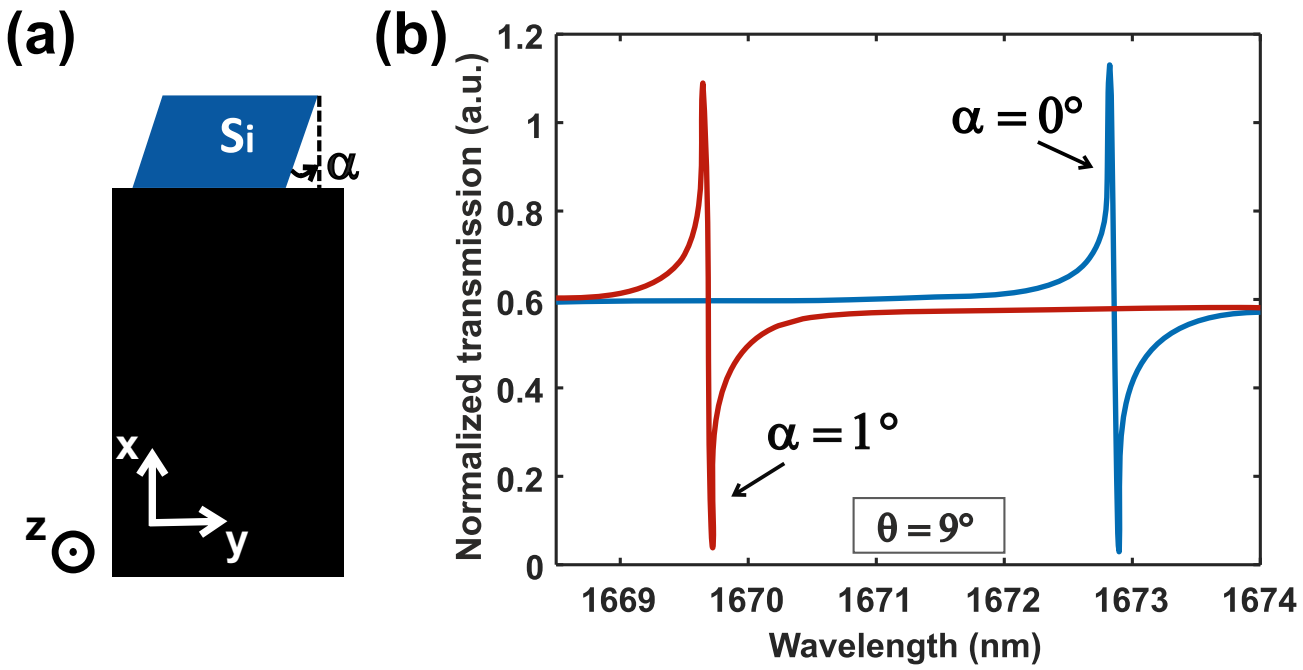

Figure 8: **a:** Diagram of a structure subjected to bending of the ridges at an angle α. **b:** Comparison of the spectral position of the quasi-BIC when $\alpha = 1°$ (red dashed line) versus $\alpha = 0°$ (green solid line) at the angle of incidence $\theta = 9°$.

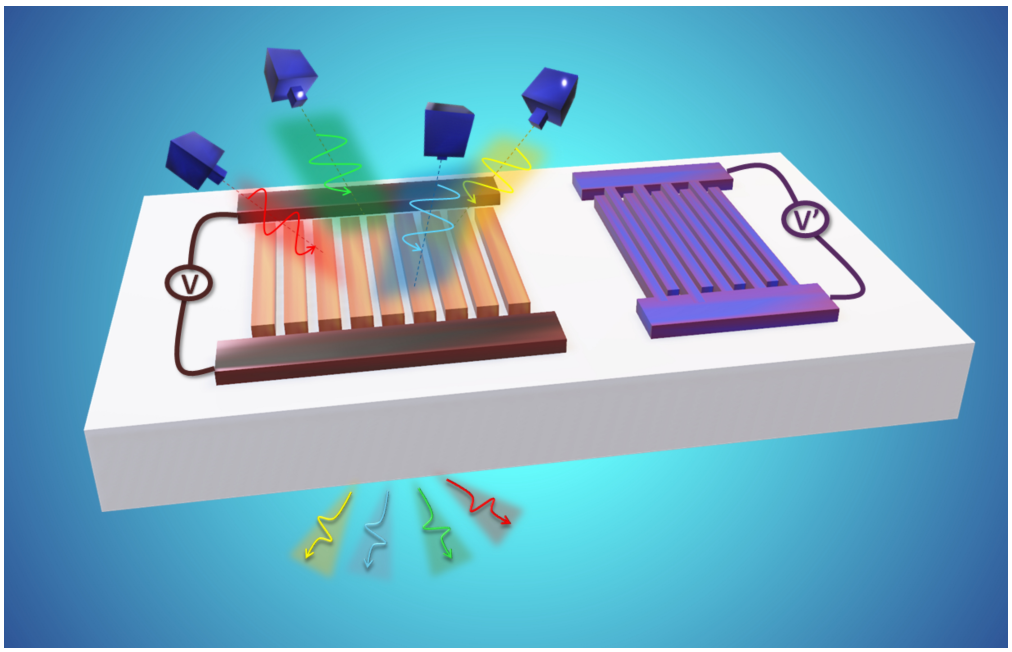

Figure 9: Artistic illustration showing the versatility of the proposed configuration.

chip-scale applications in the NIR.

Acknowledgments

Computations have been partially performed on the supercomputer facilities of the "Mésocentre de calcul de Franche-Comté". This work has been achieved in the frame of the EIPHI Graduate school (contract "ANR-17-EURE-0002) and supported by French RENATECH network through its FEMTO-ST technological facility. The authors wish to express their gratitude to Prof. Jacquot Maxime for supplying the inverted microscope that served as the foundation for the optical bench. We also extend our thanks to Ms. Lilia Arapan for her assistance and the time she dedicated to optimizing the silicon layer deposition.

Disclosures

The authors declare no conflicts of interest.

Data Availability

Data underlying the results presented in this paper are not publicly available at this time but may be obtained from the authors upon reasonable request.

References

[1] D. Dovzhenko, S. Ryabchuk, Y. P. Rakovich, I. Nabiev, Nanoscale **2018**, 10, 8 3589.

[2] L. Tao, Z. Chen, Z. Li, J. Wang, X. Xu, J.-B. Xu, InfoMat **2021**, 3, 1 36.

[3] T. J. Kippenberg, A. L. Tchebotareva, J. Kalkman, A. Polman, K. J. Vahala, Phys. Rev. Lett. **2009**, 103 027406.

[4] J. A. Schuller, E. S. Barnard, W. Cai, Y. C. Jun, J. S. White, M. L. Brongersma, Nat. Mater. **2010**, 9, 3 193.

[5] S. Jahani, Z. Jacob, Nat. Nanotechnol. **2016**, 11, 1 23.

[6] A. Figotin, I. Vitebskiy, Phys. Rev. E **2003**, 68, 3 036609.

[7] Y. Zhang, W. Liu, Z. Li, Z. Li, H. Cheng, S. Chen, J. Tian, Opt. Lett. **2018**, 43, 8 1842.

[8] S. Fan, J. D. Joannopoulos, Phys. Rev. B **2002**, 65, 23 235112.

[9] D. Marinica, A. Borisov, S. Shabanov, Phys. Rev. Lett. **2008**, 100, 18 183902.

[10] M.-S. Hwang, K.-Y. Jeong, J.-P. So, K.-H. Kim, H.-G. Park, Commun. Phys. **2022**, 5, 1 106.

[11] A. Hoblos, M. Suarez, N. Courjal, M.-P. Bernal, F. I. Baida, OSA Continuum **2020**, 3, 11 3008.

[12] A. Kodigala, T. Lepetit, Q. Gu, B. Bahari, Y. Fainman, B. Kanté, Nature **2017**, , 11;541(7636) 196.

[13] Y. Plotnik, O. Peleg, F. Dreisow, M. Heinrich, S. Nolte, A. Szameit, M. Segev, Phys. Rev. Lett **2011**, 107, 18 183901.

[14] K. Koshelev, Y. Tang, K. Li, D.-Y. Choi, G. Li, Y. Kivshar, ACS Photonics **2019**, 6, 7 1639.

[15] Z. Liu, Y. Xu, Y. Lin, J. Xiang, T. Feng, Q. Cao, J. Li, S. Lan, J. Liu, Phys. Rev. Lett **2019**, 123, 25 253901.

[16] R. Liu, C. Zhou, Opt. Lett. **2023**, 48 6565.

[17] S. Cai, S. Zong, X. Liu, G. Liu, J. Chen, Z. Liu, Applied Physics Letters **2023**, 123, 11.

[18] S. Feng, T. Liu, W. Chen, F. Wu, S. Xiao, Sci. China Phys. Mech. Astron. **2023**, 66, 124214.

[19] T. Liu, M. Qin, F. Wu, S. Xiao, Phys. Rev. B **2023**, 107 075441.

[20] M. Roussey, M.-P. Bernal, N. Courjal, D. Van Labeke, F. I. Baida, R. Salut, App. Phys. Lett. **2006**, 89, 24.

[21] C. Wang, M. Zhang, B. Stern, M. Lipson, M. Lončar, Opt. Express **2018**, 26, 2 1547.

[22] H. Weigand, V. V. Vogler-Neuling, M. R. Escalé, D. Pohl, F. U. Richter, A. Karvounis, F. Timpu, R. Grange, ACS Photonics **2021**, 8, 10 3004.

[23] M. N. Polyanskiy, Sci. Data **2024**, 11, 1 94.

[24] C. W. Hsu, B. Zhen, J. Lee, S.-L. Chua, S. G. Johnson, J. D. Joannopoulos, M. Soljačić, Nature **2013**, 499, 7457 188.

[25] J. Zhang, B. Pan, W. Liu, D. Dai, Y. Shi, Opt. Express **2022**, 30, 12 20839.

[26] F. I. Baida, J. J. Robayo Yepes, A. Ndao, J. App. Phys. **2023**, 133, 12.

[27] X. Li, J. Ma, S. Liu, P. Huang, B. Chen, D. Wei, J. Liu, Light: Science & Applications **2022**, 11, 1 317.

[28] K.-K. Wong, Properties of lithium niobate, 28. IET, **2002**.

[29] J. Parravicini, J. Safioui, V. Degiorgio, P. Minzioni, M. Chauvet, Journal of Applied Physics **2011**, 109, 3.

[30] H. Lu, B. Sadani, G. Ulliac, C. Guyot, N. Courjal, M. Collet, F. I. Baida, M.-P. Bernal, Optics express **2013**, 21, 14 16311.

[31] M. Sanz-Paz, C. Ernandes, J. U. Esparza, G. W. Burr, N. F. Van Hulst, A. Maitre, L. Aigouy, T. Gacoin, N. Bonod, M. F. Garcia-Parajo, et al., Nano letters **2018**, 18, 6 3481.

[32] K. Koshelev, A. Bogdanov, Y. Kivshar, Science Bulletin **2019**, 64, 12 836, sPECIAL TOPIC: Electromagnetic Metasurfaces: from Concept to Applications.

[33] M. Darvishzadeh-Varcheie, M. Kamandi, M. Albooyeh, F. Capolino, Optics Letters **2019**, 44, 20 4957.

[34] A. V. Kabashin, S. Patskovsky, A. N. Grigorenko, Opt. Express **2009**, 17, 23 21191.

[35] Y. Zhou, X. Li, S. Li, Z. Guo, P. Zeng, J. He, D. Wang, R. Zhang, M. Lu, S. Zhang, et al., Opt. Express **2019**, 27, 24 34788.

[36] S. Mesli, H. Yala, M. Hamidi, A. Belkhir, F. I. Baida, Opt. Express **2021**, 29, 14 21199.

[37] Z. Yu, X. Sun, Light: Science & Applications **2020**, 9, 1 1.